

## VARIABLE ACCRETION IN THE EMBEDDED PHASE OF STELLAR EVOLUTION

E. I. VOROBYOV<sup>1,2</sup>

*Accepted for publication in Astrophysical Journal*

### ABSTRACT

Motivated by the recent detection of a large number of embedded young stellar objects (YSOs) with mass accretion rates that are inconsistent with the predictions of the standard model of inside-out collapse (Shu 1977), we perform a series of numerical hydrodynamic simulations of the gravitational collapse of molecular cloud cores with various initial masses, rotation rates, and sizes. We focus on the early Class I stage of stellar evolution when circumstellar disks are exposed to high rates of mass deposition from infalling envelopes. Our numerical modeling reproduces the large observed spread in accretion rates inferred for embedded YSOs in Perseus, Serpens, and Ophiuchus star forming regions by Enoch et al. (2009), yielding 37%–75% of objects with “sub-Shu” accretion rates  $\dot{M} \lesssim 10^{-6} M_{\odot} \text{ yr}^{-1}$  and 1%–2% of objects with “super-Shu” accretion rates  $\dot{M} > 10^{-5} M_{\odot} \text{ yr}^{-1}$ . Mass accretion rates in the Class I stage have a log-normal distribution, with its shape controlled by disk viscosity and disk temperature. The spread in  $\dot{M}$  is greater in models with lower viscosity and smaller in models with higher viscosity and higher disk temperature, suggesting that gravitational instability may be a dominant cause of the observed diversity in  $\dot{M}$  in embedded YSOs. Our modeling predicts a weak dependence between the mean mass accretion rates and stellar masses in the Class I stage, in sharp contrast to the corresponding steep dependence for evolved T Tauri stars and brown dwarfs.

*Subject headings:* circumstellar matter — planetary systems: protoplanetary disks — hydrodynamics — ISM: clouds — stars: formation

### 1. INTRODUCTION

It has recently become evident that young stellar objects (YSOs) in the embedded phase of stellar evolution exhibit a variety of mass accretion rates, which range between  $\dot{M} \sim 10^{-8} M_{\odot} \text{ yr}^{-1}$  and  $\dot{M} \sim 10^{-5} M_{\odot} \text{ yr}^{-1}$  (e.g. Dunham et al. 2006; Enoch et al. 2009) and often cannot be accounted for in the standard model of inside-out collapse (Shu 1977). According to this model, the infall rate of gas from an envelope onto a star/disk system is  $\dot{M}_{\text{infall}} \approx c_s^3/G$ , where  $c_s$  is the sound speed. For the typical gas temperatures in star forming regions  $T_g=10\text{--}20$  K, the standard model predicts infall rates of order  $1.2\text{--}4.2 \times 10^{-6} M_{\odot} \text{ yr}^{-1}$ . According to Enoch et al. (2009), however, more than 50% of YSOs in Perseus, Serpens, and Ophiuchus star-forming regions have inferred mass accretion rates  $10^{-8} M_{\odot} \text{ yr}^{-1} \lesssim \dot{M} \lesssim 10^{-6} M_{\odot} \text{ yr}^{-1}$ , which are considerably lower than the infall rates. At the same time, the envelope mass decreases about as predicted by the standard model (Enoch et al. 2009), implying that the observationally inferred and theoretically derived infall rates  $\dot{M}_{\text{infall}}$  agree with each other.

The obvious mismatch between  $\dot{M}$  and  $\dot{M}_{\text{infall}}$  was first noticed by Kenyon et al. (1990) based on the comparison between typical lifetimes of embedded YSOs and inferred bolometric luminosities—the accretion luminosity  $\sim 10^{-6} - 10^{-5} M_{\odot} \text{ yr}^{-1}$  inferred from the duration of the embedded phase a few  $\times 10^5$  yr turned out to be much larger than the typical bolometric luminosity  $\sim 10^{-7} M_{\odot} \text{ yr}^{-1}$ . This “luminosity problem” can be solved by the infalling material first piling up in a

circumstellar disk and then being accreted onto a protostar mostly in short-lived FU-Ori-like episodes with accretion rates  $\dot{M} > 10^{-5} M_{\odot} \text{ yr}^{-1}$ . Numerous mechanisms for this episodic accretion have been proposed in the past. These include the thermal ionization instability (Lin & Papaloizou 1985; Hartmann & Kenyon 1985; Bell & Lin 1994), close encounters in binary systems (Bonnell & Bastein 1992), gravitational instability and fragmentation in embedded circumstellar disks (Vorobyov & Basu 2005, 2006), a combination of the magneto-rotational instability in the inner disk regions and gravitational instability in the outer disk regions (Zhu et al. 2009), and close encounters in young stellar clusters (Pfalzner et al. 2003).

Most theoretical and numerical studies of episodic accretion have been focused so far on explaining observable characteristics of the FU-Ori-like accretion bursts. In this paper, however, we mostly focus on the quiescent phase of accretion between the bursts. This phase has recently gained much interest due to a discovery of very low luminosity objects or VELLOs in dense molecular cores that have previously been thought of as “starless” (e.g. Young et al. 2002; Kauffmann et al. 2005; Bourke et al. 2006; Stecklum et al. 2007). One possible explanation for their low luminosity ( $L < 0.1 L_{\odot}$ ) is a quiescent accretion, in which  $\dot{M}$  has to be more than an order of magnitude lower than the Shu infall rates  $1.2\text{--}4.2 \times 10^{-6} M_{\odot} \text{ yr}^{-1}$ , suggesting again that the protostellar accretion history may not be as simple as predicted by the standard model.

In this paper, we provide a comprehensive study of the mass accretion rates  $\dot{M}$  and disk infall rates  $\dot{M}_{\text{infall}}$  in the embedded phase of stellar evolution (focusing mostly on the Class I stage). We use numerical hydrodynamic simulations of the cloud core collapse with a

<sup>1</sup> Institute for Computational Astrophysics, Saint Mary’s University, Halifax, B3H 3C3, Canada; vorobyov@ap.smu.ca.

<sup>2</sup> Institute of Physics, South Federal University, Stachki 194, Rostov-on-Don, 344090, Russia.

self-consistent disk formation and long-term evolution. We run a large set of model covering a wide range of cloud core masses and angular velocities. The general problem of explaining the large spread of observed protostellar accretion rates in the Class I stage is addressed using ideas from the burst mode of accretion discovered recently by Vorobyov & Basu (2005, 2006).

## 2. DESCRIPTION OF NUMERICAL MODEL

Our numerical model is similar to that used recently by Vorobyov & Basu (2009a) to simulate the secular evolution of viscous and self-gravitating circumstellar disks and the mass accretion rates in the late evolution phase of T Tauri stars (TTs) and brown dwarfs (BDs) (Vorobyov & Basu 2009b). For the reader's convenience, we briefly review the basic concept and equations.

We employ numerical hydrodynamic simulations in the thin-disk approximation to compute the evolution of rotating, gravitationally unstable cloud cores with various initial masses  $M_{\text{cl}}$  and ratios of rotational to gravitational energy  $\beta$ . We start our numerical integration in the pre-stellar phase, which is characterized by a collapsing *starless* cloud core, continue into the embedded phase of stellar evolution, which sees the formation of a star/disk/envelope system, and terminate our simulations in the late accretion phase, when most of the cloud core has accreted onto the star/disk system. Once the disk has self-consistently formed, it occupies the innermost regions of our numerical grid, while the infalling cloud core (the envelope) occupies the rest of the grid. This ensures that the mass infall rate onto the disk  $\dot{M}_{\text{infall}}$  is accurately determined by the dynamics of the gas in the envelope.

The basic equations of mass and momentum transport in the thin-disk approximation are

$$\frac{\partial \Sigma}{\partial t} = -\nabla_p \cdot (\Sigma \mathbf{v}_p), \quad (1)$$

$$\Sigma \frac{d\mathbf{v}_p}{dt} = -\nabla_p \mathcal{P} + \Sigma \mathbf{g}_p + (\nabla \cdot \mathbf{\Pi})_p, \quad (2)$$

where  $\Sigma$  is the mass surface density,  $\mathcal{P} = \int_{-Z}^Z P dz$  is the vertically integrated form of the gas pressure  $P$ ,  $Z$  is the radially and azimuthally varying vertical scale height,  $\mathbf{v}_p = v_r \hat{\mathbf{r}} + v_\phi \hat{\boldsymbol{\phi}}$  is the velocity in the disk plane,  $\mathbf{g}_p = g_r \hat{\mathbf{r}} + g_\phi \hat{\boldsymbol{\phi}}$  is the gravitational acceleration in the disk plane, and  $\nabla_p = \hat{\mathbf{r}} \partial / \partial r + \hat{\boldsymbol{\phi}} r^{-1} \partial / \partial \phi$  is the gradient along the planar coordinates of the disk. The gravitational acceleration  $\mathbf{g}_p$  includes both the gravity of a central point object (when formed) and the self-gravity of a circumstellar disk and envelope. The latter component is found by solving the Poisson integral using the convolution theorem. The viscous stress tensor  $\mathbf{\Pi}$  is expressed as

$$\mathbf{\Pi} = 2\Sigma \nu \left( \nabla v - \frac{1}{3} (\nabla \cdot \mathbf{v}) \mathbf{e} \right), \quad (3)$$

where  $\nabla v$  is a symmetrized velocity gradient tensor,  $\mathbf{e}$  is the unit tensor, and  $\nu$  is the kinematic viscosity. The components of  $(\nabla \cdot \mathbf{\Pi})_p$  in polar coordinates  $(r, \phi)$  can be found in Vorobyov & Basu (2009a).

The best candidate for viscosity in circumstellar disks is turbulence induced by the magneto-rotational instability (MRI), though other mechanisms such as non-linear hydrodynamic turbulence cannot be completely

eliminated due to the large Reynolds numbers involved. We make no assumptions about the source of viscosity and parameterize its magnitude using the usual  $\alpha$ -prescription (Shakura & Sunyaev 1973)

$$\nu = \alpha \tilde{c}_s^2 Z, \quad (4)$$

where  $\tilde{c}_s^2 = \partial \mathcal{P} / \partial \Sigma$  is the effective sound speed of (generally) non-isothermal gas. The vertical scale height  $Z$  is determined in every computational cell and at every time step of integration using an assumption of local hydrostatic equilibrium in the gravitational field of the central star and the disk (see Vorobyov & Basu 2009a).

For most of the numerical simulations in this paper, we use  $\alpha = 0.01$ . This choice is motivated by the recent work of Vorobyov & Basu (2009a), who studied numerically the secular evolution of viscous and self-gravitating disks. They found that *if* circumstellar disks around solar-mass protostars could generate and sustain turbulence than the temporally and spatially averaged  $\alpha$  should lie in the  $10^{-3} - 10^{-2}$  limits. Smaller values of  $\alpha$  ( $\lesssim 10^{-4}$ ) have little effect on the resultant mass accretion history, while larger values ( $\alpha \gtrsim 10^{-1}$ ) destroy circumstellar disks during less than 1.0 Myr of evolution and are thus unlikely from the point of view of disk longevity. We note that we have intentionally taken the largest possible value for  $\alpha$ , since we want to assess the maximum effect that viscosity may have on the accretion history in the embedded phase. The case of a smaller  $\alpha = 10^{-3}$  will be considered in brief in Section 5.2. We also note that viscosity is introduced in numerical simulations only after disk formation. In the pre-disk phase, the  $\alpha$ -parameter is set to zero.

Equations (1) and (2) are closed with a barotropic equation that makes a smooth transition from isothermal to adiabatic evolution at  $\Sigma = \Sigma_{\text{cr}} = 36.2 \text{ g cm}^{-2}$ :

$$\mathcal{P} = c_s^2 \Sigma + c_s^2 \Sigma_{\text{cr}} \left( \frac{\Sigma}{\Sigma_{\text{cr}}} \right)^\gamma, \quad (5)$$

where  $c_s = 0.188 \text{ km s}^{-1}$  is the sound speed in the beginning of numerical simulations (corresponding to the initial gas temperature of 10 K) and  $\gamma = 1.4$ . The adopted value for  $\Sigma_{\text{cr}}$  corresponds to the gas volume number density of  $10^{-11} \text{ cm}^{-3}$  for a disk in the vertical hydrostatic equilibrium at temperature 10 K. The effect of larger  $\gamma$  and, as a consequence, hotter circumstellar disks is explored in Section 5.3.

Equations (1) and (2) are solved in polar coordinates  $(r, \phi)$  on a numerical grid with  $128 \times 128$  points. We have found that an increase in the resolution to  $256 \times 256$  grid zones makes little influence on the accretion history but helps to save a considerable amount of CPU time and consider many more model cloud cores. We use the method of finite differences with a time-explicit, operator-split solution procedure similar in methodology to the ZEUS code. Advection is performed using the second-order van Leer scheme. The radial points are logarithmically spaced. The innermost grid point is located at  $r_{\text{sc}} = 5 \text{ AU}$ , and the size of the first adjacent cell varies in the 0.17–0.36 AU range depending on the cloud core size. We introduce a ‘‘sink cell’’ at  $r < 5 \text{ AU}$ , which represents the central star plus some circumstellar disk material, and impose a free inflow inner boundary condition. The outer boundary is reflecting. A small amount

of artificial viscosity is added to the code, though the associated artificial viscosity torques are always negligible in comparison with the gravitational torques.

### 3. INITIAL CONDITIONS

We start our numerical simulations from starless cloud cores, which have surface densities  $\Sigma$  and angular velocities  $\Omega$  typical for a collapsing axisymmetric magnetically supercritical core (Basu 1997)

$$\Sigma = \frac{r_0 \Sigma_0}{\sqrt{r^2 + r_0^2}}, \quad (6)$$

$$\Omega = 2\Omega_0 \left(\frac{r_0}{r}\right)^2 \left[ \sqrt{1 + \left(\frac{r}{r_0}\right)^2} - 1 \right], \quad (7)$$

where  $\Omega_0$  is the central angular velocity,  $r_0$  is the radius of central near-constant-density plateau defined as  $r_0 = kc_s^2/(G\Sigma_0)$  and  $k = \sqrt{2}/\pi$ . These initial profiles are characterized by the important dimensionless free parameter  $\eta \equiv \Omega_0^2 r_0^2 / c_s^2$  and have the property that the asymptotic ( $r \gg r_0$ ) ratio of centrifugal to gravitational acceleration has magnitude  $\sqrt{2}\eta$ . The centrifugal radius of a mass shell initially located at radius  $r$  is estimated to be  $r_{cf} = j^2/(Gm) = \sqrt{2}\eta r$ , where  $j = \Omega r^2$  is the specific angular momentum. We note that  $\eta$  is similar in magnitude to the ratio of rotational to gravitational energy  $\beta = E_{rot}/E_{grav}$ , where the rotational and gravitational energies are calculated as

$$E_{rot} = 2\pi \int_{r_{sc}}^{r_{out}} r a_c \Sigma r dr, \quad E_{grav} = -2\pi \int_{r_{sc}}^{r_{out}} r g_r \Sigma r dr. \quad (8)$$

Here,  $a_c = \Omega^2 r$  is the centrifugal acceleration, and  $r_{out}$  is the outer cloud core radius. The numerical relationship between the two parameters is  $\beta = 0.91\eta$ . The gas has a mean molecular mass  $2.33 m_H$  and cloud cores are initially isothermal with temperature  $T = 10$  K.

We present results from nine sets of models, the parameters of which are detailed in Table 1. Each set is characterized by a distinct ratio  $\beta$  of rotational to gravitational energy. The adopted values of  $\beta$  lie within the limits inferred by Caselli et al. (2002) for dense molecular cloud cores,  $\beta = (10^{-4} - 0.07)$ . The product  $r_0\Omega_0$  for every model in a given set is kept constant to enforce the  $\beta = \text{const}$  condition (the initial sound speed  $c_s = 0.188$  km s $^{-1}$  is equal for all models). In addition, the ratio  $r_{out}/r_0$  is set to 6.0 to generate gravitationally unstable truncated cores of similar form.

The actual procedure for generating a specific cloud core with a given value of  $\beta$  is as follows. First, we choose the outer cloud core radius  $r_{out}$  and find  $r_0$  from the condition  $r_{out}/r_0 = 6.0$ . Then, we find the central surface density  $\Sigma_0$  from the relation  $r_0 = \sqrt{2}c_s^2/(\pi G\Sigma_0)$  and determine the resulting cloud core mass  $M_{cl}$  from Equation (6). Finally, the central angular velocity  $\Omega_0$  is found from the condition  $\beta = 0.91\eta = 0.91\Omega_0^2 r_0^2 / c_s^2$ .

In total, we have simulated numerically the time evolution of 78 cloud cores. We note that model sets with greater  $\beta$  have on general a smaller number of models due to numerical difficulties associated with modeling of massive cloud cores with high angular velocities. The resulting initial cloud core mass function

$dN/dM_{cl} = M_{cl}^{m_1}$  has exponents  $m_1 = -0.4 \pm 0.1$  in the  $0.1 M_\odot < M_{cl} < 1.0 M_\odot$  mass range and  $m_2 = -1.3 \pm 0.2$  in the  $1.0 M_\odot < M_{cl} < 3.0 M_\odot$  range. These values are somewhat shallower than usually inferred from nearby star-forming regions (e.g. Enoch et al. 2006). The slope of the cloud core mass function varies in different star forming regions and the effect of this variation will be considered in a follow-up study.

### 4. TIME EVOLUTION OF MASS ACCRETION RATES

In this section, we review the accretion history in the early phase of stellar evolution as derived using our numerical hydrodynamic simulations. We calculate the instantaneous mass accretion rate  $\dot{M} = -2\pi r_{sc} v_{r_{sc}} \Sigma(r_{sc})$  as the mass passing through the sink cell per one time step of numerical integration (which in physical units is usually equal to 10–20 days). We note that the size of the sink cell  $r_{sc} = 5$  AU is larger than the stellar radius. The inner disk at  $r < 5$  AU may add additional variability to the accretion rates, in particular due to the thermal ionization instability (Bell & Lin 1994) or MRI (Zhu et al. 2009). These effects may somewhat alter the temporal behaviour of the actual accretion rates onto the stellar surface. Protostellar jets may also decrease the rate of mass deposition onto the star by about 10%. We leave these complicated phenomena for a future study.

Figure 1 shows the time behaviour of  $\dot{M}$  (solid lines) for 12 models characterized by distinct initial cloud core masses  $M_{cl}$  (in  $M_\odot$ ) and ratios of the rotational to gravitational energy  $\beta$ . In addition, the dashed lines present mass infall rates calculated as  $\dot{M}_{infall} = -2\pi r v_r \Sigma(r)$ , where  $r = 600$  AU. The disk radius in our models rarely exceeds 600 AU and  $\dot{M}_{infall}$  represents the rate of gas deposition from an infalling envelope onto a disk. The vertical dotted lines mark the onset of the Class I (left) and Class II (right) stages of stellar evolution, as inferred from the mass remaining in the envelope. Following a prescription of André et al. (1993) (which is most useful for numerical simulations), we assume that the Class I/Class II stages ensue when 50%/90% of the initial cloud core mass, respectively, has been accreted onto the star plus disk system. Other classification schemes may introduce a systematic shift of order unity.

The early evolution of the mass accretion rate is similar in all models— $\dot{M}$  reaches a maximum value of  $\sim 2 \times 10^{-5} M_\odot \text{ yr}^{-1}$  and then settles at a near-constant value of order of  $10^{-5} M_\odot \text{ yr}^{-1}$ . This early phase of near-constant accretion ends when the first layer of infalling material hits the centrifugal radius at 5.0 AU and a disk starts to form in our numerical simulations. The subsequent evolution of mass accretion is controlled by the physical processes in the disk and the rate of mass loading  $\dot{M}_{infall}$  onto the disk. A continuing deposition of matter from the infalling envelope, as indicated by the dashed lines in Figure 1, leads to the development of gravitational instability and fragmentation in the disk. Fragments typically form at  $r \gtrsim 40$  AU, have typical masses of up to 10–20 Jupiters, sizes of several AU, number densities of up to  $10^{13} - 10^{14} \text{ cm}^{-3}$ , and are pressure supported against their own gravity. These fragments are quickly driven into the inner disk regions via the gravitational exchange of angular momentum with the spiral arms and trigger a short-lived burst of mass accretion

TABLE 1  
 MODEL PARAMETERS

Set	$\beta$	$\Omega_0$	$r_0$	$r_{\text{out}}$	$M_{\text{cl}}$	$N$
1	$1.18 \times 10^{-3}$	0.27 – 1.00	1380 – 5180	$(0.8 - 3.0) \times 10^4$	0.8 – 3.0	8
2	$2.29 \times 10^{-3}$	0.37 – 2.24	860 – 5180	$(0.5 - 3.0) \times 10^4$	0.5 – 3.0	11
3	$3.37 \times 10^{-3}$	0.45 – 3.40	690 – 5180	$(0.4 - 3.0) \times 10^4$	0.4 – 3.0	14
4	$5.10 \times 10^{-3}$	0.53 – 6.70	410 – 5180	$(0.2 - 3.0) \times 10^4$	0.24 – 3.0	12
5	$7.25 \times 10^{-3}$	0.67 – 8.30	414 – 5180	$(0.2 - 3.0) \times 10^4$	0.24 – 3.0	9
6	$1.20 \times 10^{-2}$	1.20 – 17.0	240 – 3450	$(0.14 - 2.0) \times 10^4$	0.14 – 2.0	11
7	$1.42 \times 10^{-2}$	2.30 – 14.0	340 – 2070	$(0.2 - 1.2) \times 10^4$	0.2 – 1.2	4
8	$2.00 \times 10^{-2}$	1.60 – 22.9	240 – 3450	$(0.14 - 2.0) \times 10^4$	0.14 – 2.0	5
9	$2.90 \times 10^{-2}$	2.00 – 20.0	340 – 3450	$(0.2 - 2.0) \times 10^4$	0.2 – 2.0	4

NOTE. — All distances are in AU, angular velocities in  $\text{km s}^{-1} \text{pc}^{-1}$ , masses in  $M_{\odot}$ , and  $N$  is the number of models in each set.

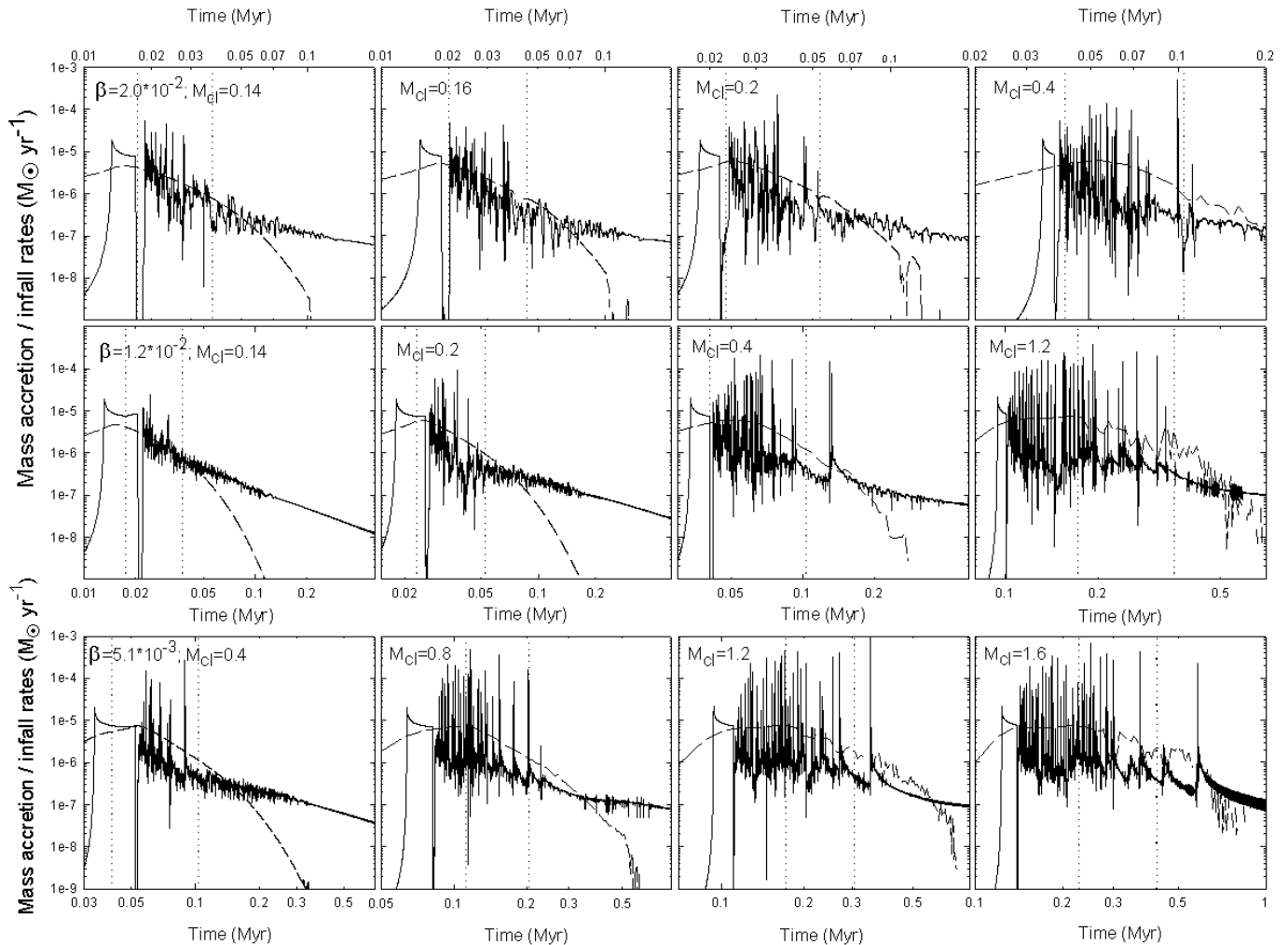


FIG. 1.— Mass accretion rates  $\dot{M}$  (solid lines) and mass infall rates  $M_{\text{infall}}$  (dashed lines) versus time elapsed since the beginning of numerical simulations. Twelve models with distinct initial cloud core masses  $M_{\text{cl}}$  (in  $M_{\odot}$ ) and ratios of rotational to gravitational energy  $\beta$  are presented. In particular, the top/middle/bottom rows have  $\beta = 2.0 \times 10^{-2}/1.2 \times 10^{-2}/5.1 \times 10^{-3}$ , respectively. The vertical dotted lines mark the onset of the Class I stage (left) and Class II stage (right) of stellar evolution.

when passing through the sink cell. This phenomenon is called the burst mode of accretion and is investigated in detail by Vorobyov & Basu (2005, 2006). The ultimate fate of the fragments is uncertain and is largely dependent on how quickly they can contract from their initial size of several AU to the planetary size to avoid tidal destruction. According to Helled et al. (2006), the contraction time for a Jupiter-mass clump to reach a central temperature of 2000 K, i.e., the temperature required to dissociate  $\text{H}_2$  to trigger rapid collapse, is  $3 \times 10^5$  yr. How-

ever, considering a fast time scale of inward radial migration to the inner 5 AU—a few tens of orbital periods at most<sup>3</sup>—we believe that most of these fragments will be tidally destroyed when approaching the central star, thus converting its gravitational energy to the accretion luminosity and producing an FU-Ori-like luminosity burst.

Figure 1 demonstrates that the burst phenomenon is

<sup>3</sup> The animation of this process can be viewed at [www.astro.uwo.ca/~vorobyov](http://www.astro.uwo.ca/~vorobyov)

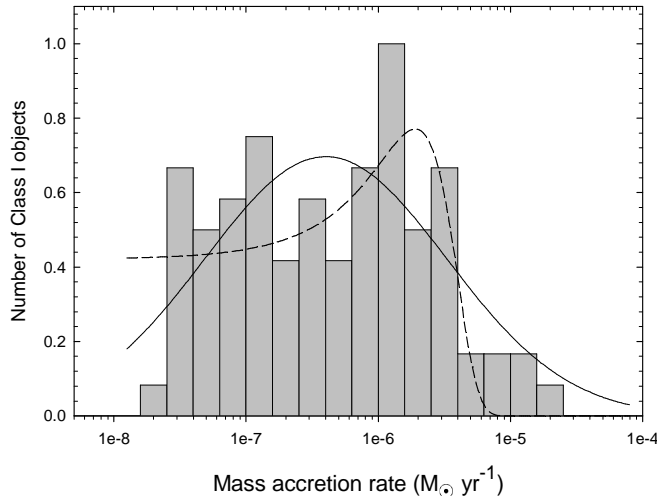


FIG. 2.— The normalized number of Class I YSOs versus mass accretion rate as inferred by Enoch et al. (2009) in Perseus, Serpens and Ophiuchus star forming regions. The solid and dashed lines are the log-normal and gaussian fits to the observed data.

more pronounced in models with greater initial cloud core masses  $M_{\text{cl}}$ . Indeed, more massive cloud cores have larger outer radii  $r_{\text{out}}$  and, as a consequence, larger centrifugal radii  $r_{\text{cf}}$ . It then follows that models with greater  $M_{\text{cl}}$  are expected to form more massive disks, which are easier susceptible to gravitational instability and fragmentation. Another important feature that can be seen in Figure 1 is that the bursts cease when the rate of mass deposition onto the disk  $\dot{M}_{\text{infall}}$  (dashed lines) falls below that of the mass accretion  $\dot{M}$  (solid lines). This clearly demonstrates the destabilizing influence that the infalling envelope has on the disk. The burst phenomenon is mostly localised to the Class 0 and Class I stages of stellar evolution, with only a few bursts taking place in the early Class II stage.

##### 5. ACCRETION VARIATIONS IN THE EMBEDDED PHASE OF STELLAR EVOLUTION

Accretion variations appear to be an intrinsic property of self-gravitating disks in the early embedded phase of stellar evolution. Young circumstellar disks, when exposed to mass deposition from infalling envelopes, undergo repeating cycles of gravitational destabilization and fragmentation. Prolonged periods of rather low accretion  $\dot{M} \lesssim 10^{-6} M_{\odot} \text{ yr}^{-1}$ , when the disk may be gravitationally unstable but is yet stable to fragmentation, are interspersed with short-lived bursts with  $\dot{M} \gtrsim 10^{-5} M_{\odot} \text{ yr}^{-1}$ , when the disk forms fragments and drives them onto the central star. It is therefore interesting to directly compare our predicted spread in  $\dot{M}$  with that inferred in YSOs in Perseus, Serpens, and Ophiuchus star-forming regions by Enoch et al. (2009). In the remaining text, we focus on the Class I stage of stellar evolution, leaving the Class 0 stage for a follow-up study.

###### 5.1. Distribution Functions of Accretion Rates

We start by constructing the distribution function (DF) of accretion rates, which shows the normalized number of YSOs versus accretion rate using data obtained by Enoch et al. (2009) in Perseus, Serpens, and Ophiuchus star-forming regions. We distribute the ob-

served accretion rates in 20 logarithmically spaced bins between  $10^{-8} M_{\odot} \text{ yr}^{-1}$  and  $10^{-4} M_{\odot} \text{ yr}^{-1}$ . The normalization is done by first finding a bin that happens to have the maximum number of YSOs and then normalizing all bins to this maximum number. The resultant normalized distribution is shown in Figure 2. The dashed/solid lines show gaussian/log-normal fits to the observed data. Neither gaussian nor log-normal functions yield good results, though the latter function is more preferable than the former. There is a lack of well defined peak in the observed accretion rates, which may to some extent be attributed to a small number of observed objects. The log-normal fit yields the following relation between the normalized number of YSOs  $N_{\text{YSO}}$  and observationally inferred accretion rates  $\dot{M}$

$$N_{\text{YSO}} = 0.7 \exp \left( -\frac{1}{2} \left[ \frac{\ln(\dot{M}/\dot{M}_0)}{2.1} \right]^2 \right), \quad (9)$$

where  $\dot{M}_0 = 4 \times 10^{-7} M_{\odot} \text{ yr}^{-1}$  is the geometric mean accretion rate. According to Enoch et al. (2009), there are approximately 55% of YSOs with sub-Shu accretion rates ( $\dot{M} < 10^{-6} \text{ yr}^{-1}$ ) and about 5% of YSOs with super-Shu rates ( $\dot{M} > 10^{-5} M_{\odot} \text{ yr}^{-1}$ ).

One feature in Figure 2 is worth special attention—there is a sizeable portion of YSOs with accretion rates smaller than  $10^{-7} M_{\odot} \text{ yr}^{-1}$ . These objects are usually characterized by bolometric luminosity  $L_{\text{bol}} < 0.1 L_{\odot}$  and constitute a group of objects called VELLOs or very low luminosity objects (e.g. Young et al. 2002; Kauffmann et al. 2005; Bourke et al. 2006; Stecklum et al. 2007). Out of 89 Class I YSOs in the compilation of Enoch et al. (2009), 19 objects are VELLOs, which is roughly 21%.

To compare our models with observations, we calculate  $\dot{M}$  every 20 yr in the Class I stage of stellar evolution. In the following text, we refer to these calculations as “accretion measurements” or simply “measurements” by analogy to observations. We note that due to the use of the sink cell in our numerical simulations, the Class I stage in some models may start before the disk begins to form (see Fig. 1). In such rare cases, accretion rates are calculated only starting from the disk formation epoch. Next, we construct the distribution function of accretion rates showing the normalized number of accretion measurements versus the accretion rate in 50 logarithmically spaced bins between  $10^{-8} M_{\odot} \text{ yr}^{-1}$  and  $10^{-4} M_{\odot} \text{ yr}^{-1}$ . The normalization is done by first finding a bin that happens to have the maximum number of accretion measurements and then normalizing all bins to this maximum number.

Figure 3 presents DFs in the Class I stage for the same set of models as in Figure 1. Model accretion rates approximately follow a log-normal distribution, the geometric mean values are mostly located in the  $0.5\text{--}1.0 \times 10^{-6} M_{\odot} \text{ yr}^{-1}$  range. There is a mild tendency for models with larger values of  $\beta$  to have a wider range of accretion rates. It is also seen that the magnitude of intrinsic variability in most models is insufficient to account for a wide spread in observed mass accretion rates (Fig. 2), implying that some object-to-object variations (in the initial cloud core masses and/or rotation rates) are needed to reproduce the observed spread.

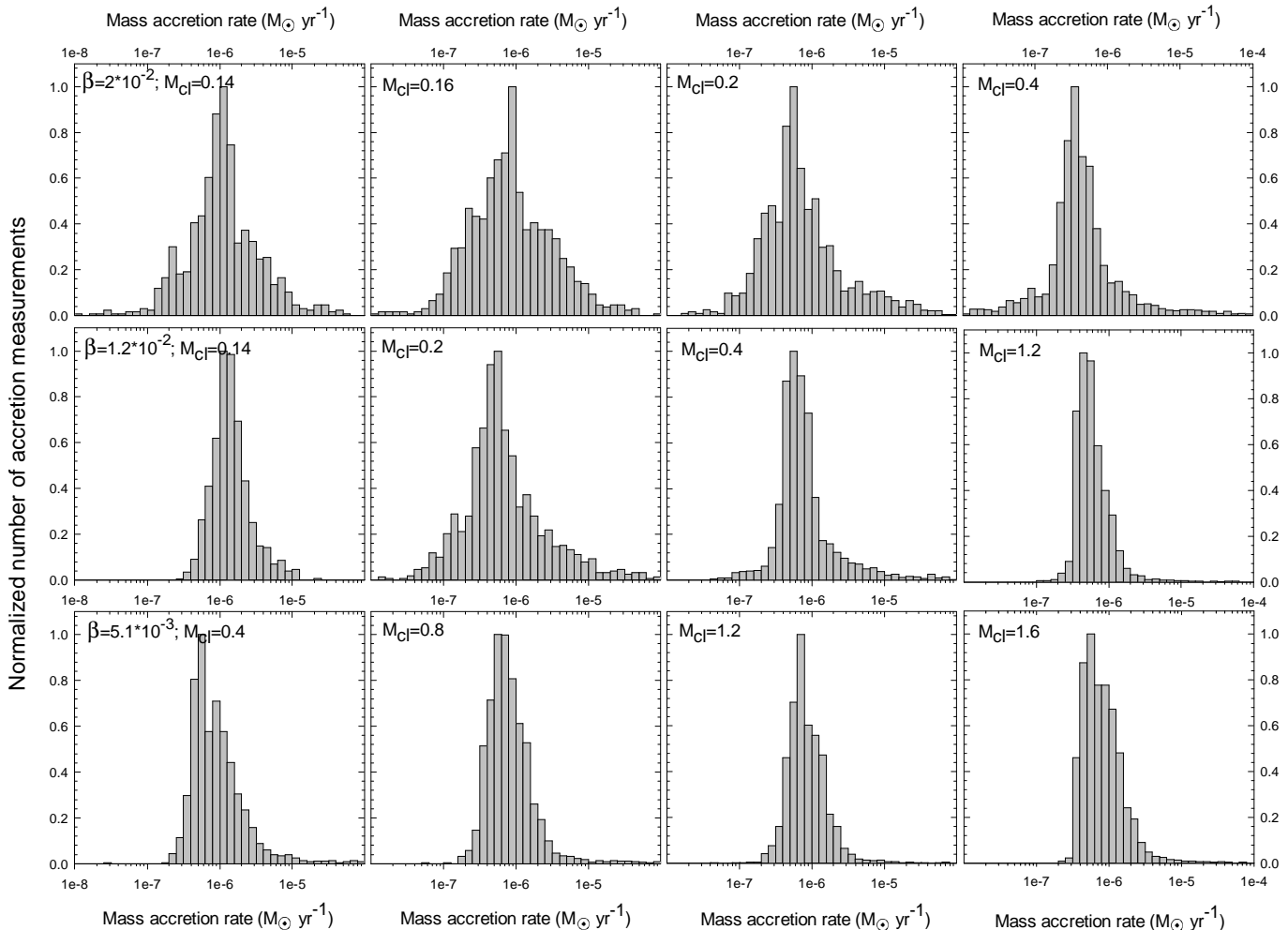


FIG. 3.— Distribution functions of accretion rates showing the normalized number of accretion measurements in the Class I stage for 12 models with the same parameters as in Figure 1.

Another interesting feature in Figure 3 is a clear trend that, for the same  $\beta$ , the peak  $\dot{M}$  decreases with increasing cloud core mass. This tendency is especially apparent for cloud cores with sufficiently high rotation rates,  $\beta \gtrsim 1.2 \times 10^{-2}$  and can be explained by a growing strength of the burst mode of accretion along the sequence of increasing cloud core masses. Indeed, Figure 1 demonstrates that, for the same  $\beta$ , the number of accretion bursts increases with increasing cloud core mass, which is explained by growing disk masses and increasing propensity of disks to fragmentation. At the same time, periods of quiescent accretion between the bursts become also more frequent and are characterized by lower rates. This acts to decrease the peak  $\dot{M}$  along the sequence of increasing cloud core masses. By the same reason, the peak  $\dot{M}$  has a weak dependence on  $\beta$  for cloud cores of similar mass.

The fact that  $\dot{M}$  in our numerical simulations are log-normally distributed is interesting. It suggests that the accretion process is not statistically independent but it has a memory effect—short periods of elevated accretion are, as a rule, followed by prolonged periods of quiescent accretion and vice versa. This pattern of time behaviour is not chaotic but is rather controlled by disk physics, implying a causal link between accretion events that are separated not too far in time.

As the next step, we want to construct the integrated DF of accretion rates, which would include data from all models in Table 1. Every individual model is characterized by a distinct duration of the Class I stage, which increases along the sequence of increasing stellar masses. This means that models with longer lifetimes of the Class I stage are more significant statistically and have a larger number of accretion measurements than models with shorter Class I lifetimes. At the same time, objects at the lower mass end (with shorter Class I lifetimes) are expected to be more abundant. The latter tendency, however, may be counterbalanced by accretion measurements biased toward more luminous (and massive) objects. Therefore, we first sum up non-normalized DFs for every models and then normalize the integrated DF in the same manner as described above, thus accentuating models with a larger number of accretion measurements.

The resultant integrated DF is presented in the upper-left panel of Figure 4. The solid line shows a log-normal fit to the model data, while the dashed line is a gaussian fit. It is evident that the log-normal function yields a much better fit to the model data than the gaussian one. In particular, we find the following relation between the normalized number of accretion measurements

$N_{\text{model}}$  and the mass accretion rates  $\dot{M}$

$$N_{\text{model}} = 0.97 \exp \left( -\frac{1}{2} \left[ \frac{\ln(\dot{M}/\dot{M}_0)}{0.75} \right]^2 \right), \quad (10)$$

where  $\dot{M}_0 = 8.8 \times 10^{-7} M_{\odot} \text{ yr}^{-1}$  is the geometric mean value. Our modeling predicts that about  $45 \pm 5\%$  of YSOs are expected to have “sub-Shu” accretion rates with  $\dot{M} \leq 10^{-6} M_{\odot} \text{ yr}^{-1}$ . Approximately the same number of YSOs are expected to have accretion rates that are roughly consistent with the standard model  $10^{-6} M_{\odot} \text{ yr}^{-1} \leq \dot{M} \leq 10^{-5} M_{\odot} \text{ yr}^{-1}$ , and only 2% of YSOs have “super-Shu” accretion rates with  $\dot{M} > 10^{-5} M_{\odot} \text{ yr}^{-1}$ . These numbers are in fare agreement with what obtained by Enoch et al. (2009). However, our numerical modeling predicts a much smaller fraction of VELLOs with  $\dot{M} < 10^{-7} M_{\odot} \text{ yr}^{-1}$ ,  $\sim 1.0\%$ , in contrast to  $\sim 21\%$  in Enoch et al. (2009). This is most likely related to the fact we have adopted too large a value for the  $\alpha$ -parameter,  $\alpha = 0.01$ , thus overemphasizing the effect of viscosity in the early disk evolution. It is known that viscosity acts to suppress gravitational instability and associated large variations in the accretion rates (Vorobyov & Basu 2009a), reducing the number and frequency of FU Orionis or VELLO events. The effect of a smaller  $\alpha$ -parameter on our model mass accretion rates is discussed below.

### 5.2. The effect of lower disk viscosity

We have considered so far model disks with  $\alpha = 10^{-2}$ . As discussed in Section 2, this value of the spatially and temporally averaged  $\alpha$ -parameter is a realistic upper limit, though some short-living fluctuations towards larger values are possible. In this section, we consider disks with an order of magnitude lower  $\alpha$ -parameter. The upper-right panel in Figure 4 presents the integrated distribution function of mass accretion rates for all models from Table 1 with  $\alpha$  set to  $10^{-3}$ . The solid line is the log-normal fit to the model data described as

$$N_{\text{model}} = 0.94 \exp \left( -\frac{1}{2} \left[ \frac{\ln(\dot{M}/\dot{M}_0)}{1.25} \right]^2 \right), \quad (11)$$

where  $\dot{M}_0 = 3.8 \times 10^{-7} M_{\odot} \text{ yr}^{-1}$ .

Numerical simulations with  $\alpha = 10^{-3}$  reveal a substantial number ( $\sim 15\%$ ) of VELLOs with  $\dot{M} \lesssim 10^{-7} M_{\odot} \text{ yr}^{-1}$ , in fare agreement with Figure 2 and data of Enoch et al. (2009). On the other hand, models with  $\alpha = 10^{-3}$  predict that about  $74 \pm 4\%$  of YSOs have sub-Shu accretion rates with  $\dot{M} \leq 10^{-6} M_{\odot} \text{ yr}^{-1}$  and only  $24 \pm 4\%$  of them have accretion rates that are consistent with the standard model  $10^{-6} M_{\odot} \text{ yr}^{-1} \leq \dot{M} \leq 10^{-5} M_{\odot} \text{ yr}^{-1}$ , in contrast to 55% and 40%, respectively, found by Enoch et al. (2009). It is evident that the  $\alpha = 10^{-3}$  models somewhat overestimate the number of sub-Shu objects as inferred from observations. This suggests that a preferable value for the temporally and spatially averaged  $\alpha$ -parameter may lie somewhere between  $10^{-3}$  and  $10^{-2}$ . In both limiting cases, about 2% of YSOs are expected to have super-Shu accretion rates with  $\dot{M} > 10^{-5} M_{\odot} \text{ yr}^{-1}$ .

### 5.3. The effect of higher disk temperature

In this section, we briefly consider the effect that a greater ratio of specific heats  $\gamma = 1.6$  may have on the mass accretion rates. An increase in  $\gamma$  in barotropic models leads to an increase in disk temperature. For instance, in the  $\gamma = 1.4$  case a mean disk temperature at  $r=10$  AU (in the Class I stage) for nine models of Figure 1 is 29–32 K, while in the  $\gamma = 1.6$  case it equals to 45–50 K. The corresponding integrated distribution function of accretion rates is shown in the lower-left panel of Figure 4. The  $\alpha$ -parameter is set to  $10^{-2}$ . As usual, the solid line is the log-normal fit to the model data described by the following relation

$$N_{\text{model}} = 1.0 \exp \left( -\frac{1}{2} \left[ \frac{\ln(\dot{M}/\dot{M}_0)}{0.68} \right]^2 \right), \quad (12)$$

where  $\dot{M}_0 = 1.4 \times 10^{-6} M_{\odot} \text{ yr}^{-1}$ . A visual comparison of the upper-left and lower-left panels demonstrates that the spread in  $\dot{M}$  in the  $\gamma = 1.6$  models is narrower than in the  $\gamma = 1.4$  case, which is a direct consequence of weaker gravitational instability in warmer disks. More specifically, there are  $37\% \pm 5\%$  sub-Shu objects and  $62\% \pm 5\%$  “standard” objects with  $10^{-6} M_{\odot} \text{ yr}^{-1} \lesssim \dot{M} \lesssim 10^{-5} M_{\odot} \text{ yr}^{-1}$ , whereas observational data indicate a prevalence of sub-Shu accretors ( $\sim 55\%$ ). The shortage of sub-Shu accretors in the  $\gamma = 1.6$  case as compared to Enoch et al. (2009) suggests that the observed circumstellar disks may be relatively cold. Alternatively, a combination of warmer disk temperature and lower turbulent viscosity (with  $\alpha \sim 10^{-3}$ ) may also provide a better fit to Enoch et al. (2009).

### 5.4. Purely viscous disks

As the last numerical experiment, we consider circumstellar disks in which mass and angular momentum transport is governed exclusively by turbulent viscosity. This is done with the purpose to investigate the role of disk self-gravity in the early embedded phase of stellar evolution. We artificially set disk self-gravity to zero immediately after disk formation, but the gravity of the central star is kept unchanged. The resultant integrated DF of accretion rates for all models of Table 1 is shown in the lower-right panel of Figure 4. Purely viscous models greatly underestimate the number of objects with “standard” accretion rates  $10^{-6} M_{\odot} \text{ yr}^{-1} \lesssim \dot{M} \lesssim 10^{-5} M_{\odot} \text{ yr}^{-1}$ . In particular, modeling predicts 7% of such objects, in contrast to  $\sim 45\%$  in the sample of Enoch et al. (2009). There are no objects with super-Shu accretion rates  $\dot{M} \gtrsim 10^{-5} M_{\odot} \text{ yr}^{-1}$ . This example serves to demonstrate the importance of disk self-gravity in the early disk evolution.

## 6. ACCRETION RATES VERSUS STELLAR MASSES

It has recently been noticed that the mass accretion rates of TTSs and BDs of 0.5–3.0 Myr age have a strong dependence on the central object mass  $M_*$  of the form  $\dot{M} \propto M_*^n$  with  $n \approx 2.0$  (see e.g. Muzerolle et al. 2003; Natta et al. 2004). A numerical model that is used in the present work can in principal reproduce this relation (Vorobyov & Basu 2009b), predicting a somewhat steeper dependence for BDs and low-mass TTSs ( $n \approx$

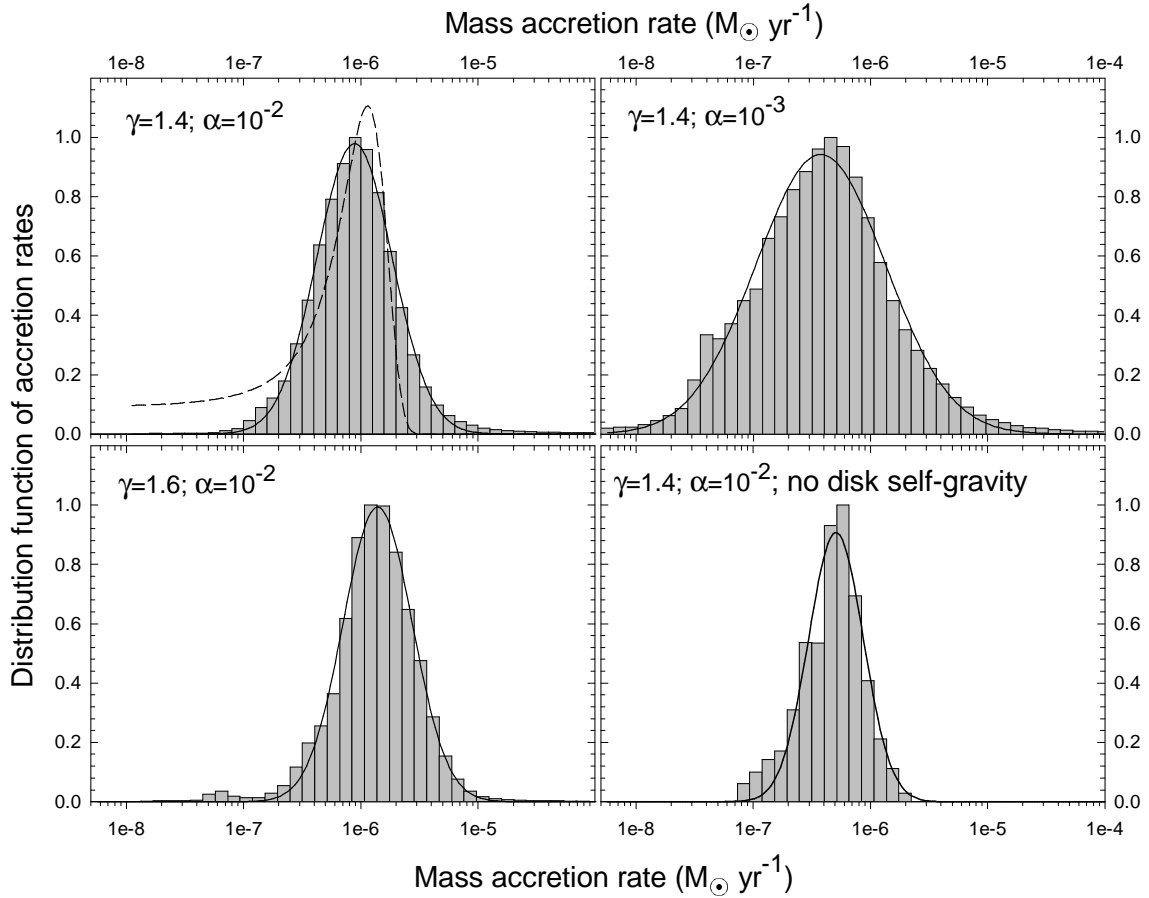


FIG. 4.— Integrated distribution function of accretion rates in the Class I stage showing the normalized number of accretion measurements  $N_{\text{model}}$  versus mass accretion rate  $\dot{M}$  for all models of Table 1. Every panel is characterized by distinct values of the  $\alpha$ -parameter and the ratio of specific heats  $\gamma$  as indicated. In addition, the lower-right panel has disk self-gravity artificially set to zero. The solid and dashed lines are the log-normal and gaussian fits to the model data, respectively.

$2.9 \pm 0.5$ ), as observed, and a shallower dependence for intermediate- and upper-mass TTSSs ( $n \approx 1.5 \pm 0.1$ ), as also observed. It is therefore very interesting to see if a similar relation is expected in the early embedded phase of stellar evolution.

For every model from Table 1, we calculate the geometric mean mass accretion rate  $\dot{M}_{\text{g.m.}}$  as a value at which the corresponding DF of accretion rates reaches a maximum. All models in this section have  $\alpha$  and  $\gamma$  set to  $10^{-2}$  and 1.4, respectively. Color symbols in Figure 5 present  $\dot{M}_{\text{g.m.}}$  (in  $M_{\odot} \text{ yr}^{-1}$ ) versus time-averaged stellar masses  $\langle M_{*} \rangle$  (in  $M_{\odot}$ ) in the Class I stage of stellar evolution. The time-averaging is done over the duration of the Class I stage, which is distinct in each model. (In particular, model set 1 is plotted by red squares, model set 2—by blue triangles-up, model set 3—by green diamonds, model set 4—by black triangles-down, model set 5—by cyan circles, model set 6—by red diamonds, model set 7—by green triangles up, model set 8—by blue diamonds, and model set 9—by black circles. Each filled symbol (of same color and shape) within a given set of models represents an individual object, which has formed from a cloud core of distinct mass, rotation rate, and size.

In addition, each filled symbol is assigned vertical bars describing (for a given model) a typical range of mass accretion rates in the Class I stage. Defining these typical values turned out not trivial. This is because some of the models may show transient drops or rises in  $\dot{M}$ , which are

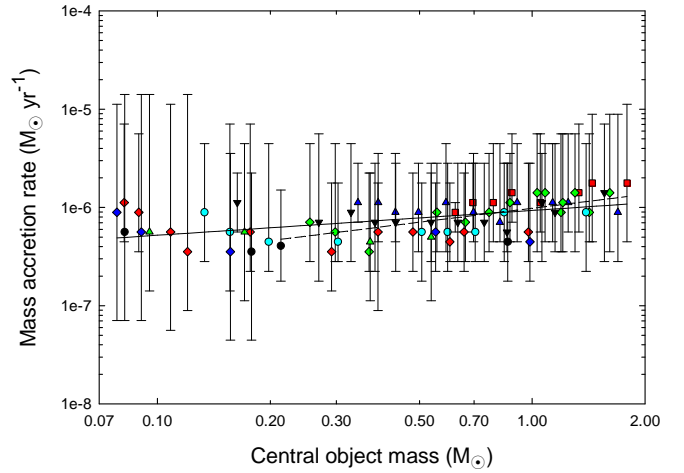


FIG. 5.— Geometric mean mass accretion rates versus time-averaged stellar masses in the Class I stage of stellar evolution. Symbols of specific shape and color represent different sets of models as described in the text (see online version for the color figure). Vertical bars delineate typical variations in the mass accretion rate in every model. The lines are the least-squares best fits to all data (solid) and intermediate- and upper-mass objects (dashed).

very short-lived and thus are not statistically significant. Therefore, the vertical bars comprise only those accretion rates the DF for which is greater than 0.05. This means that we have excluded objects with extreme accretion rates, which have probability to be detected less than



one part in twenty. Considering the number of detected objects along the line of constant central object mass ( $\lesssim 20$ ) in Enoch et al. (2009), we believe that our estimate represents conservative values.

Figure 5 clearly demonstrates that the mass accretion rates in the embedded phase do *not* show any strong dependence on the stellar mass. The least-squares best fit to all data (solid line) yields the following relation

$$\dot{M}_{\text{g.m.}} = 10^{-6} \langle M_* \rangle^{0.25 \pm 0.05}, \quad (13)$$

which is considerably shallower than that for the TTSS and BDs. Accretion rates of the intermediate- and upper-mass objects ( $M_* \gtrsim 0.2 M_\odot$ ) in Figure 5 seem to have a somewhat steeper dependence on  $\langle M_* \rangle$ , as indicated by the dashed line, yet the corresponding exponent  $0.5 \pm 0.1$  is considerably smaller than that of the evolved TTSS and BDs of 0.5–3.0 Myr age. We again want to emphasize that our model does reproduce a steep dependence seen in TTSS and BDs for both purely self-gravitating disks (Vorobyov & Basu 2008) and self-gravitating disks with turbulent viscosity (Vorobyov & Basu 2009b).

A hint as to why this difference takes place can be seen in Figure 1. The embedded phase is characterized by mass infall rates onto the disk  $\dot{M}_{\text{infall}}$  (dashed lines) that are often greater than the mass accretion rate onto the star (solid lines). This implies that accretion in the embedded phase may in part be controlled by the rate of gas deposition onto the disk, which in turn is expected to be only weakly dependent on the stellar mass.

We demonstrate this in Figure 6, which shows the time-averaged infall rates  $\langle \dot{M}_{\text{infall}} \rangle$  (filled circles) versus time-averaged stellar masses  $\langle M_* \rangle$  for most models in Table 1. We have eliminated some of the models, which happen to have disk radii that exceed 600 AU—the radius at which we calculate the mass infall rate. The time-averaging is done over the duration of the Class I stage. For comparison, we also plot the geometric mean mass accretion rates  $\bar{M}$  (open circles). Note that we use the same symbol type for all models in this figure. It is evident that  $\langle \dot{M}_{\text{infall}} \rangle$  is *systematically* greater than  $\bar{M}$ . The least squares fit yields the following relation between the time-averaged infall rates and stellar masses

$$\langle \dot{M}_{\text{infall}} \rangle = 4.0 \times 10^{-6} \langle M_* \rangle^{0.20 \pm 0.03}, \quad (14)$$

the exponent of which is quite similar to that of the  $\bar{M}_{\text{g.m.}}$  vs.  $\langle M_* \rangle$  relation (dashed line, see also equation [13]). A weak dependence of  $\langle \dot{M}_{\text{infall}} \rangle$  on the stellar mass is explained by a gradual increase in the envelope temperature along the sequence of increasing stellar masses. We also emphasize that our model infall rates lie within the limits predicted by the standard model of Shu (1977) for star forming regions with gas temperature  $T_g = 10 - 25$  K.

## 7. CONCLUSIONS

In this paper, we have studied mass accretion rates on to the star  $\dot{M}$  and mass infall rates onto the disk  $\dot{M}_{\text{infall}}$  in the early embedded phase of stellar evolution, focusing on objects with stellar masses lying in the 0.08–2.0  $M_\odot$  range. We have employed numerical hydrodynamic simulations of the gravitational collapse of a large number of model cloud cores, which cover a wide range of masses,

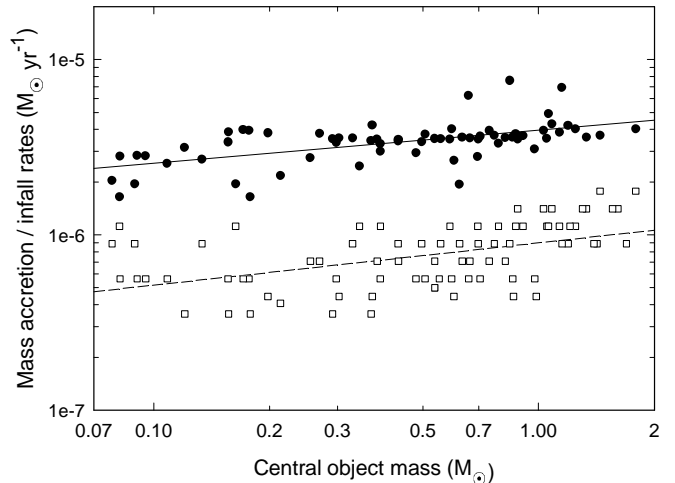


FIG. 6.— Geometric mean mass accretion rates onto the star  $\bar{M}_{\text{g.m.}}$  (open squares) and time-averaged mass infall rates onto the disk ( $\dot{M}_{\text{infall}}$ ) (filled circles) versus time-averaged stellar masses in the Class I stage of stellar evolution. Most models from Table 1 are shown in the figure. The dashed and solid lines are the least squares best fits to  $\bar{M}_{\text{g.m.}}$  and  $\langle \dot{M}_{\text{infall}} \rangle$ , respectively.

initial rotation rates, and sizes. The numerical integration is started in the *pre-stellar* phase and followed into the late accretion phase when almost all of the initial cloud core has been accreted onto the star/disk system. We compare our model accretion rates with those recently inferred from observations of embedded YSOs in young star forming regions. We find the following.

- Our numerical modeling yields a highly variable accretion history in the phase that immediately follows disk formation. Prolonged periods of low accretion  $\dot{M} \lesssim 10^{-6} M_\odot \text{ yr}^{-1}$ , when disks may be gravitationally unstable but are yet stable to fragmentation, are interspersed with short-lived bursts of mass accretion with  $\dot{M} \gtrsim 10^{-5} M_\odot \text{ yr}^{-1}$ , when disks form fragments and drive them onto the central star via the exchange of angular momentum with spiral arms. The latter phenomenon is called the burst mode of accretion and is investigated in detail in Vorobyov & Basu (2006).
- Model accretion rates  $\dot{M}$  in the early embedded phase have a log-normal distribution, with its shape depending on the magnitude of turbulent viscosity (parameterized using the usual  $\alpha$ -model of Shakura & Sunyaev (1973)) and disk temperature.
- The spread in  $\dot{M}$  (or the width of the accretion rate distribution function) is greater in models with lower  $\alpha$  and smaller in models with higher  $\alpha$  and higher disk temperature  $T_d$ . An increase in either  $T_d$  or  $\alpha$  (or both) acts to stabilize disk against gravitational instability (Vorobyov & Basu 2009a). This suggests that gravitational instability may be a dominant cause of the accretion diversity in circumstellar disks exposed to a continuing gas deposition from infalling envelopes.
- Our models yield a large population of objects (37%–75%) with mass accretion rates  $\dot{M} \lesssim$

$10^{-6} M_{\odot} \text{ yr}^{-1}$ , which are smaller than those predicted by the standard model of inside-out collapse, a few  $\times 10^{-6} M_{\odot} \text{ yr}^{-1}$  (Shu 1977). A similar large fraction of embedded YSOs with sub-Shu accretion rates ( $\sim 55\%$ ) was recently reported by Enoch et al. (2009) for Perseus, Serpens, and Ophiuchus star forming regions.

- Approximately 1%-2% of objects in our modeling have super-Shu accretion rates  $\dot{M} > 10^{-5} M_{\odot} \text{ yr}^{-1}$ , which is roughly a factor of 2-3 smaller than found by Enoch et al. (2009). This suggests that other (than disk fragmentation) mechanisms may also contribute to bursts of mass accretion in the embedded phase stellar evolution.
- Purely viscous models, with disk self-gravity artificially set to zero, significantly underestimate the number of objects with “standard” mass accretion rates  $10^{-6} M_{\odot} \text{ yr}^{-1} \lesssim \dot{M} \lesssim 10^{-5} M_{\odot} \text{ yr}^{-1}$ , yielding essentially no objects with super-Shu rates. This demonstrates the importance of disk self-gravity in the early disk evolution.
- Mean mass accretion rates in the early embedded phase show only a weak dependence on the time-averaged stellar masses of the form  $\dot{M}_{\text{g.m.}} = 10^{-6} \langle M_{*} \rangle^{0.25 \pm 0.05}$ , in sharp contrast to the steep (with exponent  $\sim 2.0$ ) empirical relation inferred for evolved TTSs and BDs of 0.5-3.0 Myr age (see

e.g. Muzerolle et al. 2003; Natta et al. 2004). This result is particularly interesting since our numerical model can reproduce the steep relation in the late evolution phase for both purely self-gravitating disks (Vorobyov & Basu 2008) and self-gravitating disks with turbulent viscosity (Vorobyov & Basu 2009b).

- The lack of strong dependence of  $\dot{M}_{\text{g.m.}}$  on  $\langle M_{*} \rangle$  in the early embedded phase can be attributed to a continuing deposition of matter from the infalling envelope. The time-averaged rate of mass infall onto the disk  $\langle \dot{M}_{\text{infall}} \rangle$  is systematically greater (roughly by a factor of four) than the mean mass accretion rate onto the star  $\dot{M}_{\text{g.m.}}$ , implying that  $\dot{M}_{\text{g.m.}}$  is at list partly determined by  $\langle \dot{M}_{\text{infall}} \rangle$ . At the same time,  $\langle \dot{M}_{\text{infall}} \rangle$  exhibits only a weak growth along the sequence of increasing stellar masses, which is caused by a moderate increase in the envelope temperature from  $\sim 10$  K to  $\sim 25$  K.

The author gratefully thanks the anonymous referee for a helpful report and Prof. Shantanu Basu for stimulating discussions. The author gratefully acknowledges present support from an ACEnet Fellowship. Numerical simulations were done on the Atlantic Computational Excellence Network (ACEnet).

#### REFERENCES

- André, P., Ward-Thompson, D., & Barsony, M. 1993, *ApJ*, 406, 122
- Basu, S. 1997, *ApJ*, 485, 240
- Bell, K. R., & Lin, D. N. C. 1994, *ApJ*, 427, 987
- Bonnell, I., & Bastien, P. 1992, *ApJ*, 401, L31
- Bourke, T. L., et al. 2006, *ApJL*, 649, 37
- Caselli, P., Benson, P. J., Myers, P. C., & Tafalla, M. 2002, *ApJ*, 572, 238
- Dunham, M. M. et al. 2006, *ApJ*, 65, 945
- Enoch, M. L., Eet al. 2006, *ApJ*, 638, 293
- Enoch, M. L., Evans II, N. J., Sargent, A. I., and Glenn, J. 2009, *ApJ*, 692, 973
- Evans, N. J. II, et al. 2009, *ApJSS*, 181, 321
- Hartmann, L., & Kenyon, S. J. 1985, *ApJ*, 299, 462
- Helled, R., Podolak, M., & Kovetz, A. 2006, *Icarus*, 185, 64
- Kauffmann, J., et al. 2005, *Astron. Nachr.*, 326, 878
- Kenyon, S. J., Hartmann, L. W., Strom, K. M., Strom, S. E. 1990, *ApJ*, 99, 869
- Lin, D. N. C., Papaloizou, J. C. B. 1985, in *Protostars and Planets II*, eds. D. C. Black and M. C. Matthews (Tucson: University of Arizona Press), 981
- Muzerolle, J., Hillenbrand, L., Calvet, N., Briceño, C., & Hartmann, L. 2003, *ApJ*, 592, 266
- Natta, A., Testi, L., Muzerolle, J., Randich, S., Comeron, F., & Persi, P. 2004, *A&A*, 424, 603
- Pfalzner, S., Tackenberg, J., & Steinhausen, M. 2008, *A&A*, 487, L45
- Shakura, N. I., & Sunyaev, R. A. 1973, *A&A*, 24, 337
- Shu, F. H. 1977, *ApJ*, 214, 488
- Stecklum, B., Melnikov, S. ., Meusinger, H. 2007, *A&A*, 463, 621
- Vorobyov, E. I., 2009, *ApJ*, 692, 1609
- Vorobyov, E. I., & Basu, S. 2005, *ApJL*, 633, L137
- Vorobyov, E. I., & Basu, S. 2006, *ApJ*, 650, 956
- Vorobyov, E. I., & Basu, S. 2008, *ApJL*, 676, 139
- Vorobyov, E. I., & Basu, S. 2009a, *MNRAS*, 393, 822
- Vorobyov, E. I., & Basu, S. 2009b, *ApJ*, in press (astro-ph:0908.1285)
- Young, C. H. et al. 2004, *ApJSS*, 154, 396
- Zhu, Z., Hartmann, L., & Gammie, C. F. 2009, 694, 1045